Detector Level ABI Spectral Response Function: FM4 analysis and comparison to other ABI modules.

Boryana Efremova[a], Aaron J. Pearlman[b], Frank Padula[b], and Xiangqian Wu[c]

[a] ERT, Inc. Laurel, MD 20707 USA USA
[b] GeoThinkTank LLC, Alexandria, VA 22314 USA
[c] NOAA, NESDIS, STAR, College Park, MD 20740 USA

ABSTRACT

A new generation of imaging instruments Advanced Baseline Imager (ABI) is to be launched aboard the Geostationary Operational Environmental Satellites - R Series (GOES-R). Four ABI flight modules (FM) are planned to be launched on GOES-R,S,T,U, the first one in the fall of 2016. Pre-launch testing is on-going for FM3 and FM4. ABI has 16 spectral channels, six in the visible/near infrared (VNIR $0.47 - 2.25\,\mu$m), and ten in the thermal infrared (TIR $3.9 - 13.3\,\mu$m) spectral regions, to be calibrated on-orbit by observing respectively a solar diffuser and a blackbody. Each channel has hundreds of detectors arranged in columns. Operationally one Analytic Generation of Spectral Response (ANGEN) function will be used to represent the spectral response function (SRF) of all detectors in a band. The Vendor conducted prelaunch end-to-end SRF testing to compare to ANGEN; detector specific SRF data was taken for: i) best detector selected (BDS) mode - for FM 2,3, and 4; and ii) all detectors (column mode) - for four spectral bands in FM3 and FM4. The GOES-R calibration working group (CWG) has independently used the SRF test data for FM2 and FM3 to study the potential impact of detector-to-detector SRF differences on the ABI detected Earth view radiances. In this paper we expand the CWG analysis to include the FM4 SRF test data - the results are in agreement with the Vendor analysis, and show excellent instrument performance and compare the detector-to-detector SRF differences and their potential impact on the detected Earth view radiances for all of the tested ABI modules.

Keywords: GOES-R, ABI, Prelaunch, Spectral Response Function (SRF)

1. INTRODUCTION

The Advanced Baseline Imager (ABI) is the primary instrument to be carried on board the GOES-R series satellites for imaging Earth's weather, climate, oceans and the environment. ABI will observe the Earth in 16 spectral bands (compared to five on current GOES) and will provide much better spatial and temporal resolution than the current GOES imager. The spectral response functions (SRF) of the six reflective and ten thermal channels are shown in the left and right panels of Figure 1 respectively. See [1] for detailed description of the ABI spectral bands heritage and design. There are four ABI units, the first flight module (FM1) is scheduled to be launched on GOES-R in November 2016. The last unit (FM4) is to be launched on GOES-U in 2025.

Together with improved spectral and spatial resolution GOES-R ABI will also have great improvement in terms of radiometric calibration, noise, and calibration stability. Similarly to its sister instrument Advanced Himawari Imager (AHI) on board Japan Meteorological Agency (JMA), Himawari-8 [2], ABI will carry a black body (BB) for calibration of the thermal channels and a solar diffuser (SD) for calibration of the reflective channels. Detailed pre-launch testing, characterization and calibration was conducted by the instrument Vendor. The pre-launch testing of all units will be concluded with the completion of FM4 testing at the end of Aug. 2016.

In this paper we focus on the ABI FM4 end-to-end detector level spectral response testing performed by the Vendor. Each ABI spectral channel consists of hundreds of detector rows and several redundant detector columns - only one detector is operated from each column. Operationally one Analytic Generation of Spectral Response (ANGEN) function - constructed by combining the transmittance/reflectance of all optical elements

Send correspondence to B.E.: E-mail: boryana.efremova@noaa.gov

Earth Observing Systems XXI, edited by James J. Butler, Xiaoxiong (Jack) Xiong, Xingfa Gu, Proc. of SPIE
Vol. 9972, 99720S · © 2016 SPIE · CCC code: 0277-786X/16/$18 · doi: 10.1117/12.2238090

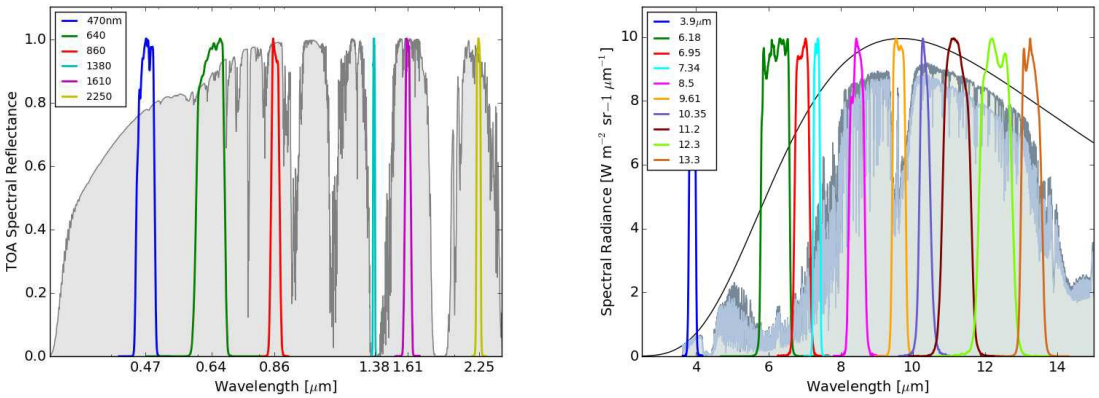

Figure 1. ABI spectral bands. Left panel: Reflective channels shown over top of the atmosphere reflectance. The central wavelengths are as follows: 0.47, 0.64, 0.86, 1.38, 1.61, 2.25 μm. Right panel: Thermal channels shown over BB spectrum at T=300K (black), and IASI spectra of ocean (blue) and vegetation (green). The central wavelengths are as follow: 3.9, 6.185, 6.95, 7.34, 8.5, 9.61, 10.35, 11.2, 12.3, 13.3 μm.

such as mirrors, beamsplitters, windows, bandpass filters, as well as detectors quantum efficiency measured by the instrument developer on component level - will be used to represent the spectral response function (SRF) of all detectors in a band. However characterizing any detector to detector SRF differences can provide useful information for anomaly resolution and image enhancement on orbit - the low instrument noise may allow small effects due to each detector having slightly different SRF to be observed in the imaging and appear as striping. Striping impacts L2 algorithms such as cloud masks and Sea Surface Temperature (SST) [3]. As discussed by [4] and [5] SRF effects could be the cause for the striping observed in SST-input channels in VIIRS. Thus studying the effects of detector specific SRF differences may facilitate the understanding and characterization of detector-to-detector striping and the development of mitigation algorithms.

The GOES-R calibration working group (CWG), which has the responsibility to provide long-term instrument science support to the GOES-R program that ensures well calibrated and navigated GOES-R L1b data for the life time of the instruments, independently assessed the SRF test data for ABI FM2 and FM3 to study the potential impact of detector-to-detector SRF differences on the ABI detected Earth view radiances [6] and [7].

In this paper we extend the same approach to the ABI FM4 system level SRF test; explore potential calibration differences due to SRF effects using typical calibrator and Earth-scene spectra to evaluate such potential effects on the ABI imaging and compare the test results to the other ABI units.

The paper is organized as follows: The results from CWG processing of the end-to-end spectral response test data for FM4 are discussed in Section 2. A brief description of the methodology used to evaluate the SRF effects is given in Section 3. The reflective channels SRFs are discussed in more detail in Section 4 and the thermal channels in Section 5. Summary and compared to other flight modules are given in Section 6.

2. ABI FM4 END-TO-END SRF TEST

The ABI FM4 system level spectral response test was conducted by the instrument Vendor in 2015, similarly to the testing of FM2 and FM3 discussed in [6] and [7]. During the test the ABI performs a slow-speed north south (NS) scan of a slit illuminated by a monochromator. The wavelength is stepped in small increments and the collection is repeated until the required ABI spectral band-pass (slightly beyond the 1% response) is covered. Stares at the internal blackbody (BB) are used to subtract offset and background emission which is significant factor in the thermal channels. A well characterized reference detector is used to correct for source drift during the test. All bands were tested in BDS mode (best detector select - only one detector is tested for each channel). In addition B12 (9.61μm), B14 (11.2μ m) B15(12.3μm), and B16(13.3μm) were tested in column mode - SRF

data was collected for each detector column separately; column 1 was collected five times (in between every other column collect) to provide information about the test repeatability.

CWG independently processed FM4 high level end-to-end SRF test data provided by the ABI Vendor; the results are in agreement with the Vendor analysis. As the test was conducted in ambient environment the channels sensitive to atmospheric absorption were influenced, the data for the most heavily affected channles (6.185, 6.95, 7.34, 8.5 μm) is not discussed in this paper.

An example of the measured individual spectral response for one reflective channel (0.47μm) is shown in Figure 2. The min/max envelope of individual SRF is shown on the left together with the ANGEN SRF which is used operationally to derive calibration parameters. In the right panel the SRFs of all individual detectors are shown. An example for individual SRF of a thermal channel (13.3μm) is shown in Figure 3. The colors and lables are as in Figure 2.

These two channels represent the variety in resutls from end-to-end SRF testing - from the channel showing one of the smallest SRF variation between detectors (0.47μm), to the one showing the largest(13.3μm).

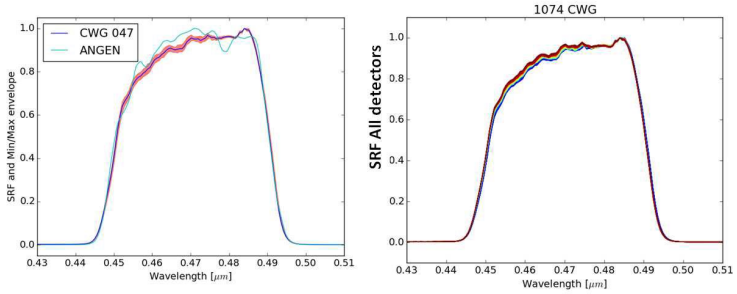

Figure 2. Example of results from detector specific SRF measurements for 0.47μm channel. Left panel: ANGEN (blue) shown over the detector specific SRF min/max envelope. Right panel: Detector specific SRF for each detector.

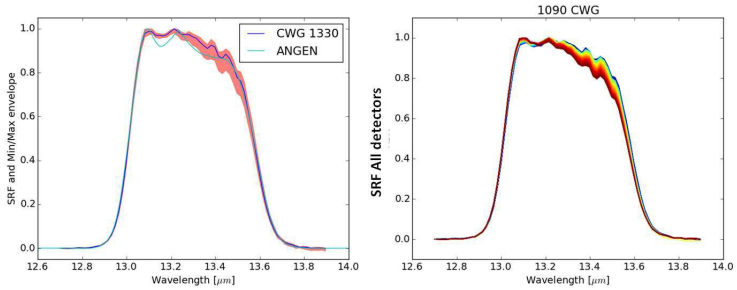

Figure 3. Example of results from detector specific SRF measurements for 13.3μm channel. Left panel: ANGEN (blue) shown over the detector specific SRF min/max envelope. Right panel: Detector specific SRF for each detector.

In order to quantify the derived SRF differences several metrics were computed. The central wavelength is defined as the average between the red and blue 50% response limits: $\lambda_C = 0.5(\lambda_{50\%blue} + \lambda_{50\%red})$. As expected it behaves similarly to the effective wavelength which is the average wavelength weighted by the spectral response function: $\lambda_{eff} = \int \lambda SRF(\lambda)d\lambda / \int (SRF(\lambda)d\lambda$. The behavior of the line-width metrics is also similar, the full width at half maximum (FWHM) is well correlated with the equivalent width $EW = \int SRF(\lambda)d\lambda$. The central wavelength λ_C maximum variation between detectors is shown in Figure 4 for all the regarded channels and is also listed in the second row of Table 1. The difference of the central wavelength to the ANGEN central wavelength is given in the third row of Table 1. Six of the ten thermal channels are listed, as for the 6.18, 6.9, 7.3, and 8.5 μm channels the derived SRF is heavily influenced by atmospheric absorption features.

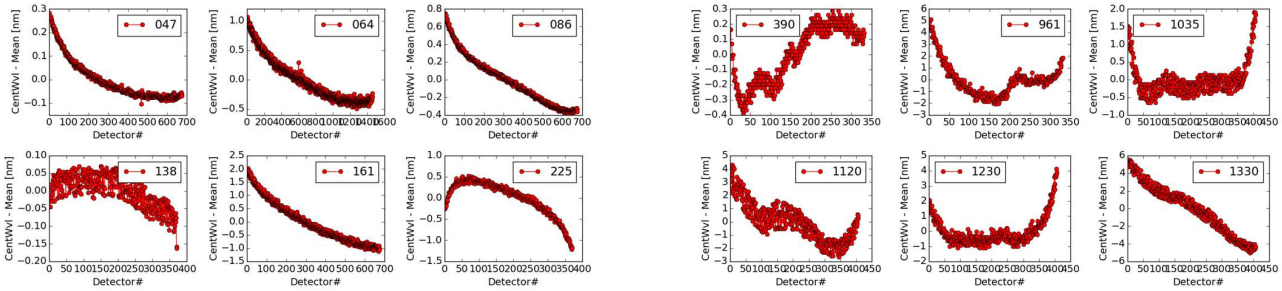

Figure 4. Central wavelength shift between detectors derived from the end-to-end SRF test. Left panel: Reflective channels; Right panel: Thermal channels.

Band	**0.47**	**0.64**	**0.86**	**1.38**	**1.61**	**2.25**	**3.9**	**9.61**	**10.35**	**11.20**	**12.30**	**13.30**
$(\lambda_{C\ MAX} - \lambda_{C\ MIN})$ **[nm]**	0.4	1.6	1.1	0.2	3.1	1.7	0.7	7.2	2.5	6.9	5.2	10.6
$\lambda_C - \lambda_{C\ ANGEN}$ **[nm]**	0.25	0.56	-0.5	-0.17	-0.25	-0.6	2.2	-4.7	-6.	-5.5	-12.8	0.3

Table 1. Shift in central wavelength between detectors (second row) and to ANGEN (third row).

For all channels the central wavelength difference to ANGEN is on the order of or smaller than the wavelength calibration error as provided by the Vendor. The detector to detector differences along the focal plane for some channels seem to exceed the estimated uncertainty. The end-to-end test taken in column mode shows some offsets in the central wavelength between the different columns, and between the repeated collects of column 1, however the slope along the detector rows is consistent between all columns taken. An example of results from column mode end-to-end SRF test collects for the 13.3μm channel is shown in Figure 5. The effective wavelength seems to be more stable (better column to column repeatability), however this is not necessarily the case for other channels.

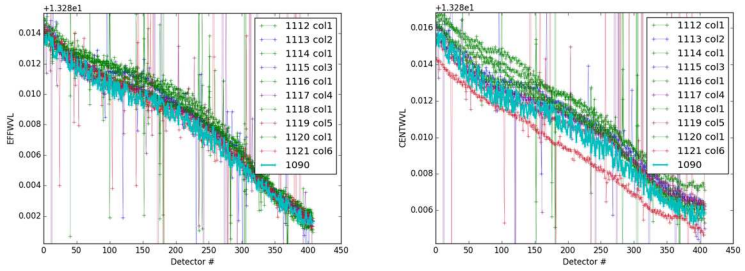

Figure 5. Example of results from column mode end-to-end SRF test collects for 13.3μm channel. The effective wavelength is shown on the left, and the central wavelength on the right. The repeated takes of column 1 are shown in green, and the BDS mode collect in light blue as indicated in the legend.

3. METHODOLOGY

In this section a brief summary of the methodology used to evaluate the potential impact of SRF differences between detectors, as measured by the end-to-end SRF testing, on ABI FM4 imaging is given.

Operationally one SRF function (ANGEN) is used to derive the calibration scource radiance, and calibration coefficients for all detectors in a channel. Alternatively detector specific SRF could be used to derive the calibration coefficients. We use both approaches to propagate the SRF detector to detector differences into the retrieved scene radiances, accounting for on-orbit calibration, and compare the results of calibrating using band average SRF vs individual SRF. There is no attempt made to simulate realistic instrument response in terms of noise and other potential causes for detector-to-detector striping apart from SRF effects.

If detector specific SRF is used to derive the calibrationi coefficients the radiance retrieved by an ideal instrument would match in source radiance observed by this detector, so the SRF differences may cause striping as each detector observes a slightly different part of the scene spectrum unless the scene spectrum is flat.

Using band average SRF to derive the calibration coefficients introduces a factor in the calibration which brings the radiance observed by the individual detectors to the average for the channel. This however is the case only if the scene spectrum perfectly matches the spectrum of the calibration target, which is often not the case, so the striping caused by SRF differences is not always reduceable by this approach.

The equation describing the spectral part of the calibration coefficients using both detector specific and band-average SRF is shown below, as well as an illustration of how it propagates the detector specific SRF effects into the retrieved scene radiances.

The detector output of the i-th detector after background subtraction (dn_i) in a linear detector response approximation is proportional to the source spectral radiance $L(\lambda)$ weighted by the detector specific spectral response SRF_i (see for example [8]):

$$dn_i = C_i \int L(\lambda) SRF_i(\lambda) d\lambda, \tag{1}$$

where C_i is a constant specific for each detector accounting for maximum quantum efficiency, system transmittance and aperture geometry factors. In order to calibrate the instrument, a calibration source (CS) of known radiance ($L_{CS}(\lambda)$) is used (a BB for thermal channels and solar irradiance reflected off a SD for the reflective channels), and a calibration coefficient M is derived relating the measured detector output (dn_{iCS}) to the band-average CS radiance ($\overline{L_{CS}}$). To compute the calibration coefficient the band average radiance is derived theoretically from the known calibration source radiance. As mentioned earlier a band-average SRF (SRF_{AV}) is used operationally to represent the spectral channel, so the CS band average radiance is the same for all detectors and equal to:

$$\overline{L_{CS}} = \frac{\int L_{CS}(\lambda) SRF_{AV}(\lambda) d\lambda}{\int SRF_{AV}(\lambda) d\lambda}, \tag{2}$$

so for the calibration coefficient using Eq.(1) and Eq.(2) we derive:

$$M_{i\ AV} = \frac{\overline{L_{CS}}}{dn_{iCS}} = \frac{1}{C_i \int L_{CS}(\lambda) SRF_i(\lambda) d\lambda} \frac{\int L_{CS}(\lambda) SRF_{AV}(\lambda) d\lambda}{\int SRF_{AV}(\lambda) d\lambda}, \tag{3}$$

or if we multiply and divide the right side by the equivalent width of the detector specific SRF_i we obtain:

$$M_{i\ AV} = \frac{1}{C_i \int SRF_i(\lambda) d\lambda} \frac{\overline{L_{CS}}}{\overline{L_{i\ CS}}}, \tag{4}$$

where $\overline{L_{i\ CS}}$ is the band-average CS radiance averaged using individual detector SRF_i.

Then, when we observe the studied Earth scene the detector output $dn_{i\ scene}$ would be as in Eq.(1), where L is the scene radiance L_{scene}. And the retrieved scene radiance from the $i-th$ detector $L_{i\ AV\ retr\ scene}$ (the AV subscript indicates that the calibration coefficient M_{AV} was used to retrieve the scene radiance) is:

$$L_{i\ AV\ retr\ scene} = M_{i\ AV} dn_{i\ scene} = \frac{C_i \int L_{scene}(\lambda) SRF_i(\lambda) d\lambda}{C_i \int SRF_i(\lambda) d\lambda} \frac{\overline{L_{CS}}}{\overline{L_{i\ CS}}} \tag{5}$$

$$L_{i\ AV\ retr\ scene} = \overline{L_{i\ scene}} \frac{\overline{L_{CS}}}{\overline{L_{i\ CS}}} \tag{6}$$

If on the other hand a detector specific SRF_i is used to derive the calibration coefficient $M_{i\ SP}$ the average CS radiance in the Eq.(4) will cancel and,

$$M_{i\ SP} = \frac{1}{C_i \int SRF_i(\lambda) d\lambda}, \tag{7}$$

$$L_{i\ SP\ retr\ scene} = \overline{L_{i\ scene}} \tag{8}$$

so the retrieved scene radiance will be exactly the band average radiance truly seen by this given detector (again we are considering an ideal instrument with only SRF differences causing detector-to-detector retrieved radiance differences).

As shown above, using average SRF to derive the calibration coefficients (M_{AV}) introduces the term $\frac{\overline{L_{CS}}}{\overline{L_{i\ CS}}}$ in the retrieved radiance, while if the M_{SP} coefficient derived using detector specific SRF_i is used the retrieved radiance would be exactly the true radiance observed by this detector. The image produced using such calibration though might still have striping, as $\overline{L_{i\ scene}}$ vary (due to SRF differences) unless the scene spectrum is flat over the wavelength range of the channel.

The M_{AV} coefficients would correct striping as long as the slope of the scene spectrum is similar to the calibration spectrum so the term $\frac{\overline{L_{CS}}}{\overline{L_{i\ CS}}}$ corrects for the ratio between average radiance seen by all detectors and detector specific radiance. If however the scene spectrum differs significantly in shape from the calibration spectrum striping due to SRF differences will not be corrected and may be even amplified. Striping may also be introduced in the case of spectrally flat scenes if the calibrator spectrum has significant slope over the spectral range covered by the channel.

In the following sections an attempt was made to quantify these effects using the results from end-to-end SRF test described in Section 2 and a subsample from the library of IASI and AVIRIS spectra of typical Earth scenes compiled by Padula at al.[9] as shown in Figure 6.

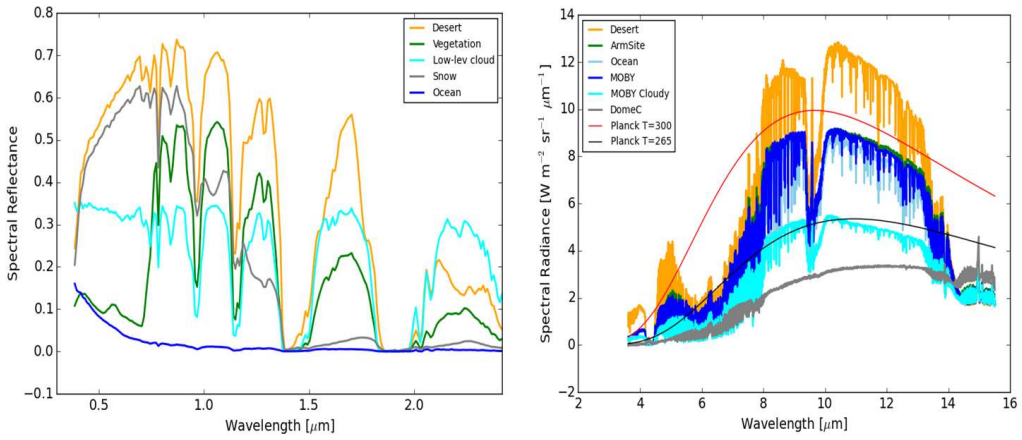

Figure 6. Left panel: Typical earth scene AVIRIS reflectance spectra from [9] used in this study for reflective channels; Right panel: Typical earth scene IASI spectra from [9] used in this study for the emissive channels. BB spectra of 300K (calibration source temperature for ABI thermal channels) and 265K are also shown. Colors are as shown in the legend.

4. DISCUSSION OF REFLECTIVE CHANNELS

In this section the effects of the measured by the end-to-end test SRF differences on the reflective channels calibration is described.

As a first step, in an attempt to check if the end-to-end test measured SRF differences can be confirmed by other data taken by the instrument we looked at the calibration coefficients derived by the reflective channels

calibration test, where calibration coefficients are derived by using an integrating sphere equipped with tungsten bulbs and covering each channels' dynamic range by 10 points in radiance. The derived coefficients show some variation between different detectors, which if dominated by spectral effects should be reproduceable by using the individual spectral response derived from the end-to-end test, and applying it as shown in Eq.(4). As measurements of the integrating sphere spectral radiance are not available, a BB spectrum at T=3000K was used to model the average calibrating source radiance ratio ($\frac{\overline{L_{CS}}}{L_{i\ CS}}$) in Eq.(4). The result does not correlate well with the variation of the linear calibration coefficients (the nonlinear term is very small and for many detectors of many channels is 0) suggesting that detector to detector SRF variations are not the primary mechanism driving calibration coefficient variation. One exception is the 1.38μm channel which shows qualitatively a similar shape as the calibration coefficients, however the amplitude caused by SRF variation is much smaller.

As a next step we calculated band-average retrieved radiances $L_{i\ SP\ retr\ scene}$ and $L_{i\ AV\ retr\ scene}$ for each detector following Eq.(8) and Eq.(6) respectively for all reflective channels using a library of AVIRIS spectra compiled in [9]. The scene spectra used are shown in the left panel of Figure 6. The result (as ratio to the average retrieved radiance) is shown in Figures 7 and 8.

The detector to detector SRF variations have small effect for most of the reflective channels except 1.61μm where it results in a radiance variation of about 1.5% for desert and snow scenes. The signal in the 1.38 channel is faint, so the noise is expected to dominate the SRF effects.

Using detector specific vs average SRF for calibration appears to have little impact on all reflective channels.

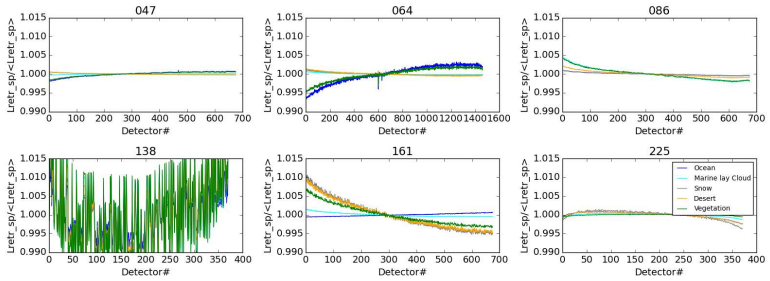

Figure 7. Effects of SRF variation on retrieved scene radiance derived from Eq.(8). The colors are as follows: yellow - desert; green - vegetation; blue - clear ocean; light blue - clouds; gray - snow.

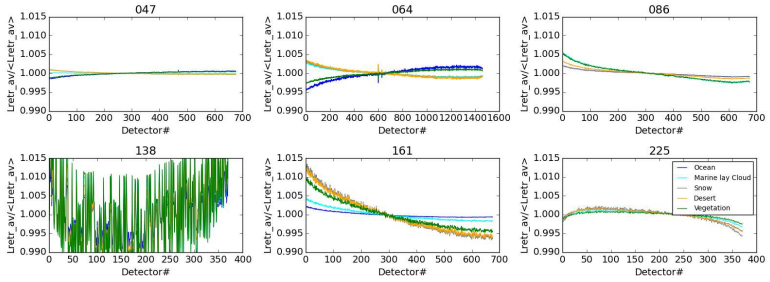

Figure 8. Effects of SRF variation on retrieved scene radiance derived from Eq.(6). The colors are as follows: yellow - desert; green - vegetation; blue - clear ocean; light blue - clouds; gray - snow.

5. DISCUSSION OF EMISSIVE CHANNELS

In this section the effects of the SRF differences on the thermal channels calibration is described.

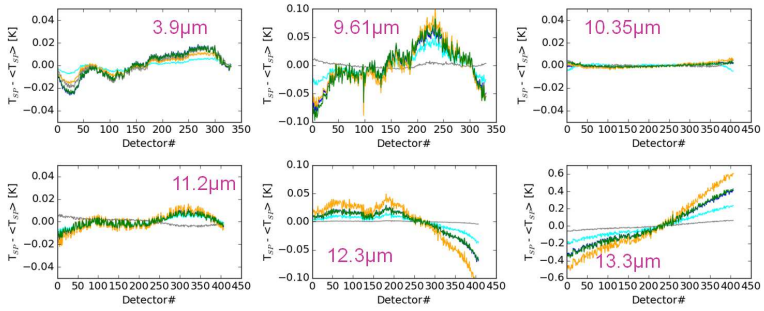

Figure 9. Effects of SRF variation on retrieved scene temperature. Radiance derived from Eq.(8). The colors are as follows: yellow - desert; green - vegetation; blue - clear ocean; light blue - cloudy ocean; gray - DomeC

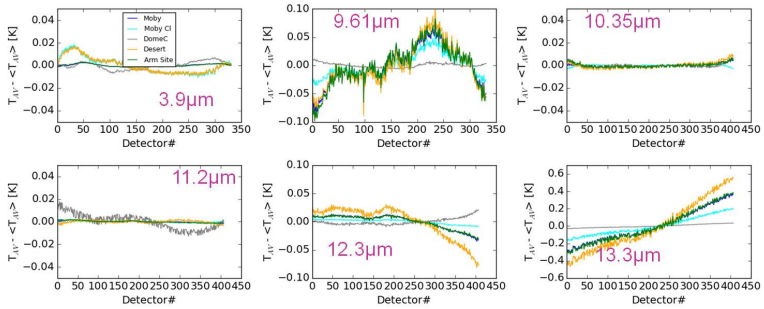

Figure 10. Effects of SRF variation on retrieved scene temperature. Radiance derived from Eq.(6). The colors are as follows: yellow - desert; green - vegetation; blue - clear ocean; light blue - cloudy ocean; gray - DomeC

Similarly to the reflective channels there is no apparent correlation between the calibration coefficients derived by the Vendor during the emissive channels calibration test and the SRF contribution calculated from Eq.(4) using the end-to-end SRF test results. One exception is the 13.30μm channel which shows qualitatively a similar shape as the calibration coefficients, however the amplitude caused by SRF variation is much smaller. Again, as in the reflective channels the variation of the calibration coefficients is much larger than can be explained by just spectral effects using the end-to-end SRF test data.

The band-average retrieved radiances $L_{i\ SP\ retr\ scene}$ and $L_{i\ AV\ retr\ scene}$ were also calculated following Eq.(8) and Eq.(6) respectively for the regarded thermal channels using the library of IASI spectra [9] shown in the right panel of Figure 6. The result (after converting to brightness temperature) is shown in Figures 9 and 10.

The end-to-end spectral response test for thermal channels has larger uncertainties; we evaluate the effects of the measured detector to detector SRF differences in order to illustrate the calibration effects of using band-average vs detector specific SRF on different scenes qualitatively, however the magnitude of the effect observable on-orbit is hard to predict due to the presence of atmosphere and larger uncertainties of the test.

The strongest effect SRF effect is in the 13.3μm channel where it yields about 1K temperature difference along the focal plane for desert scenes. Comparison between Figures 9 and 10 gives an illustration of the effects of calibrating using individual (Fig. 9) vs band-average (Fig. 10) SRF. For some channels the average SRF decreases the temperature differences among detectors, however the effect is scene-dependent - for example, while temperature differences of the higher emissivity scenes in the 11.2μm channel are improved the DomeC scene shows larger temperature differences when calibrated using band-average SRF. For other channels, most notably the 13.3μm channel there is no significant difference between the two calibration methods. The 9.61μm channel results are not influenced by the calibration method, as it is situated over the plateau of the T=300K calibrating source spectrum and SRF differences have no effect.

Similar results were observed in the ABI FM2 and FM3 testing - the 13.30μm channel showed similar trends of about 1K over high emissivity earth scenes [6],[7].

6. SUMMARY

The ABI FM4 end-to-end spectral test results show some SRF variations along the detector arrays as well as central wavelength shifts with respect to the band average SRF ANGEN which will be used operationally. The shifts are mostly within the stated wavelength uncertainties of the test, however if biases are found once the instrument is on orbit the SRF testing data can be used for verification.

The detector to detector SRF variations measured by the end-to-end test are small for most reflective channels except 1.61μm where they yield a radiance variation of about 1.5% for desert and snow scenes.

The end-to-end spectral response test for thermal channels has larger uncertainties, so we evaluate the effects of the measured detector to detector SRF differences in order to illustrate the calibration effects of using band-average vs detector specific SRF on different scenes qualitatively, however our demonstration should not be interpreted as a prediction of the magnitude of the effect to be observed on orbit. The effect of SRF differences measured by the end-to-end test propagated into retrieved scene temperature is strongest in the 13.30μm channel where it yields about 1K temperature difference along the focal plane for desert scenes. Similar results were observed in the ABI FM2 and FM3 testing - the 13.30μm channel showed similar trend.

Operationally ANGEN is used to derive the calibration source radiance, and calibration coefficients for all detectors in a channel. Alternatively detector specific SRF could be used to derive the calibration coefficients. We applied both approaches to propagate the SRF detector to detector differences into the retrieved scene radiances, accounting for on-orbit calibration. The comparison shows that the approach yielding less striping is scene dependent (see Figures 9 and 10), making it hard to pick a best method to suppress striping.

ACKNOWLEDGMENTS

The authors thank the ABI instrument vendor and members of the wider CWG, PWG, and Flight groups for insights shared during many productive discussions. This work is funded by the GOES-R Program. The manuscript contents are solely the opinions of the authors and do not constitute a statement of policy, decision, or position on behalf of NOAA or the U.S. government.

REFERENCES

[1] Schmit, T. J., Gunshor, M. M., Menzel, W. P., Gurka, J. J., Li, J., and Bachmeier, A. S., "Introducing the next-generation advanced baseline imager on goes-r," *Bulletin of the American Meteorological Society* **86**(8), 1079–1096 (2005).

[2] Okuyama, A., Andou, A., Date, K., Hoasaka, K., Mori, N., Murata, H., Tabata, T., Takahashi, M., Yoshino, R., and Bessho, K., "Preliminary validation of himawari-8/ahi navigation and calibration," *Proc. SPIE* **9607**, 96072E–96072E–10 (2015).

[3] Bouali, M. and Ignatov, A., "Adaptive reduction of striping for improved sea surface temperature imagery from suomi national polar-orbiting partnership (s-npp) visible infrared imaging radiometer suite (viirs)," *Journal of Atmospheric and Oceanic Technology* **31**(1), 150–163 (2014).

[4] Padula, F. and Cao, C., "Detector-level spectral characterization of the suomi national polar-orbiting partnership visible infrared imaging radiometer suite long-wave infrared bands m15 and m16," *Appl. Opt.* **54**, 5109–5116 (Jun 2015).

[5] Wang, Z. and Cao, C., "Assessing the effects of suomi npp viirs m15/m16 detector radiometric stability and relative spectral response variation on striping," *Remote Sensing* **8**(2), 145 (2016).

[6] Pearlman, A. J., Padula, F., Cao, C., and Wu, X., "The goes-r advanced baseline imager: detector spectral response effects on thermal emissive band calibration," *Proc. SPIE* **9639**, 963917–963917–7 (2015).

[7] Padula, F. and Cao., C., "Goes-r abi detector-level spectral response function performance characterization.," *IGARSS* (2015).

[8] Datla, R., Shao, X., Cao, C., and Wu, X., "Comparison of the Calibration Algorithms and SI Traceability of MODIS, VIIRS, GOES, and GOES-R ABI Sensors," *Remote Sensing* **8**, 126 (Feb. 2016).
[9] Padula, F. and Cao., C., "Using s-npp viirs as a transfer radiometer to inter-compare goes-r abi and himawari-8 ahi," *AMS* (2014).